Published on 22 March 2022. Downloaded by Ulsan National Institute of Science & Technology (UNIST) on 4/25/2022 10:19:47 AM.

Energy & Environmental Science

ROYAL SOCIETY OF CHEMISTRY

PAPER

View Article Online
View Journal

Check for updates

Cite this: DOI: 10.1039/d1ee03861c

Interface rich CuO/Al_2CuO_4 surface for selective ethylene production from electrochemical CO_2 conversion†

Siraj Sultan, ‡[a] Hojeong Lee, ‡[a] Sojung Park, ‡[b] Minho M. Kim,‡[c] Aram Yoon, ‡[de] Hansaem Choi, [a] Tae-Hoon Kong, [a] Young-Jin Koe,[f] Hyung-Suk Oh, [f] Zonghoon Lee, *[de] Hyungjun Kim,*[c] Wooyul Kim *[b] and Youngkook Kwon *[a]

Received 13th December 2021,
Accepted 21st March 2022

DOI: 10.1039/d1ee03861c

rsc.li/ees

The electrochemical reduction of carbon dioxide (CO_2) to multicarbon hydrocarbons or oxygenate compounds beyond carbon monoxide is of great importance, as it offers a promising way to obtain a renewable fuel of high energy density and close the carbon cycle. Copper has been considered the predominant and effective electrocatalyst for the CO_2 reduction reaction (CO_2RR), especially when aiming for ethylene products. However, the selectivity or current density of most catalysts for ethylene production is not satisfactory at competitive prices. Here, we present a newly designed electrocatalyst comprising Al_2CuO_4 nanosheets uniformly covered with CuO nanoparticles (CuAl-**1**: CuO/Al_2CuO_4-23) by phase and interphase engineering, achieving an ultrahigh selectivity of 82.4% for ethylene in an H-cell system with good catalytic stability and material durability for 100 h. In a flow-cell electrolyzer, this catalyst achieves a remarkably high ethylene partial current density of 421 mA cm^{-2}, substantially higher than the as-synthesized bare CuO (261 mA cm^{-2}) counterpart. The results of time-resolved attenuated total reflection-surface enhanced infrared absorption spectroscopy (ATR-SEIRAS) suggest that compared to the CuO catalyst, CuAl-**1** enabled high surface coverages of *CO intermediates and strengthened adsorption of *CO for C–C coupling toward *OCCO, which is an intermediate for the production of ethylene. X-ray absorption analysis confirms that Cu oxide species in CuAl-**1** are well retained during CO_2 reduction, whereas the bare CuO catalyst is completely reduced to the metallic Cu state. Density functional theory calculations propose that a synergistic effect between CuO and Al_2CuO_4 in the CuAl-**1** steers the CO_2RR pathway towards ethylene.

Broader context

The conversion of greenhouse CO_2 gas into value-added carbon-based fuels and feedstocks by an electrochemical CO_2 reduction reaction (CO_2RR) is a potentially promising approach to reduce the level of CO_2 in the earth's atmosphere and store sustainable energy. To improve the economic viability of the CO_2RR in industrial applications, the electrosynthesis of ethylene or ethanol products from CO_2 is desired due to their high demand in the global market. However, the production of ethylene or ethanol products from the CO_2RR is often challenged by the low selectivity of most catalysts toward C_{2+} products. Thus, the design of an efficient and inexpensive catalyst that can direct the CO_2 electroreduction pathway toward a specific desired C_{2+} product is the key of the CO_2RR. In this study, we present an effective and scalable "phase and interphase engineering" approach for the development of a new and powerful CO_2RR electrocatalyst composed of Al_2CuO_4 nanosheets uniformly covered with CuO nanoparticles (CuO/Al_2CuO_4: having abundant CuO and Al_2CuO_4 interface) to achieve the superior and selective generation of ethylene from electrochemical CO_2 conversion. During the CO_2RR, these CuO/Al_2CuO_4 interface sites allowed high surface coverage of *CO intermediates and strengthened the adsorption of *CO for C–C coupling toward *OCCO, allowing the CO_2 electroreduction pathway to be tuned for specific ethylene formation.

[a] School of Energy and Chemical Engineering, Ulsan National University of Science and Technology (UNIST), Ulsan 44919, Republic of Korea. E-mail: ykwon@unist.ac.kr
[b] Department of Energy Engineering / KENTECH Institute for Environmental and Climate Technology, Korea Institute of Energy Technology (KENTECH), Naju 58330, Republic of Korea. E-mail: wkim@kentech.ac.kr
[c] Department of Chemistry, Korea Advanced Institute of Science and Technology (KAIST), Daejeon 34141, Republic of Korea. E-mail: linus16@kaist.ac.kr
[d] Department of Materials Science and Engineering, UNIST, Ulsan 44919, Republic of Korea. E-mail: zhlee@unist.ac.kr
[e] Center for Multidimensional Carbon Materials, Institute for Basic Science (IBS), UNIST, Ulsan 44919, Republic of Korea
[f] Clean Energy Research Center, Korea Institute of Science and Technology (KIST), Seoul 02792, Republic of Korea

† Electronic supplementary information (ESI) available. See DOI: 10.1039/d1ee03861c

‡ These authors contributed equally to this work.

Published on 22 March 2022. Downloaded by Ulsan National Institute of Science & Technology (UNIST) on 4/25/2022 10:19:47 AM.

Introduction

The excessive emission of anthropogenic carbon dioxide (CO_2) gas from the combustion of traditional fossil fuels causes many serious environmental problems, such as global warming, which hinders the growth and the development of our modern industrial society.[1–3] Thus, how to effectively reduce the level of CO_2 in the atmosphere has become a global challenge. One potential approach to this problem is the conversion of CO_2 gas into value-added fuels and feedstocks by an electrochemical CO_2 reduction reaction (CO_2RR); this conversion process not only reduces the level of CO_2 in the earth's atmosphere but also stores sustainable energy.[4–6] Currently, the main dominant and selective products of the CO_2RR process are mostly limited to two-electron-reduced carbon monoxide (CO) or formic acid (HCOOH),[7–11] while the production of further reduced C_1 products such as methane (CH_4)[12,13] or methanol (CH_3OH)[14–16] has also been reported with high faradaic efficiency (FE). However, among the various CO_2RR products, the more reduced C_2 products, such as ethylene (C_2H_4), which are formed through multiple electron–proton transfer intermediates and complex C–C bond coupling reactions are highly desirable due to their larger energy density and high market price, but the selective generation of C_2H_4 from the CO_2RR remains a challenging problem.[17,18]

To date, copper (Cu) is the only transition metal-based CO_2RR electrocatalyst that can produce multi-carbon hydrocarbons with appreciable selectivity.[19,20] However, bulk Cu catalysts suffer from several limitations, such as high overpotentials, poor selectivity toward a specific C_2 product, deactivation issues, low catalytic activity due to limited active surface area and losses of FE caused by a concurrent hydrogen evolution reaction (HER).[17,21,22] Up until now, various kinds of strategies and techniques have been extensively used to improve the selectivity of C_2H_4 on the Cu catalysts, including tailoring the physiochemical properties of Cu through heteroatom doping,[23] construction of Cu nanostructures with different particle sizes and morphologies,[24–26] facet dependency,[27] alloying of Cu with noble metals[28,29] and production of grain boundaries and nanoscale defects in Cu nanosheets to create more catalytic active sites for adjusting the reaction intermediates/pathways in the CO_2RR.[30,31] But still, the selectivity of most of the catalysts reported for C_2H_4 is not satisfactory to be applicable for practical implementation. Thus, the design of an electrocatalyst for the selective generation of ethylene that meets the criteria for the large-scale commercialization of the electrochemical CO_2RR system is necessary and urgent.

Given that the surface-bound CO dimer intermediate through C–C coupling reaction is the key species for C_2H_4 formation, $Cu^{\delta+}$ ($Cu^{\delta+}$ has vacant 3d orbitals and therefore have a moderate CO* binding energy) has been suggested as an active surface for CO dimerization in Cu-catalysts.[32–34] Indeed, reasonably good activity and selectivity for C_2H_4 generation have been achieved through introducing $Cu^{\delta+}$ sites in Cu-catalysts. Similarly, copper–oxide has been found as a promising electrocatalyst for CO dimerization through the C–C coupling reaction and C_2H_4 generation.[32–34] Unfortunately, $Cu^{\delta+}$ or Cu–oxide catalysts suffer from low C_2H_4 selectivity or are very likely to be reduced under CO_2RR conditions; in particular, the electrosynthesis of C_2 compounds requires high applied reduction potentials in which $Cu^{\delta+}$ or Cu–oxide leads to the inactive metallic state Cu and the catalysts probably loses the ability of C–C coupling for the formation of C_2 products within the first few hours of reaction.[23,27] With this consideration, we assume that the introduction or supporting of Cu–oxide or $Cu^{\delta+}$ on or into modifier elements (for example, Al has a $2s^2 2p^1$ electron configuration, the empty orbital of Al tends to take electrons from Cu that tune and shifts the valence state of Cu oxide for a more positive redox potential) could not only increase the formation of C_2 products beyond their optima but also improve the stability of the $Cu^{\delta+}$ or Cu–oxide in a lasting fashion.

To this end, here we present a new electrocatalyst composed of Cu–oxide nanoparticles (CuO NPs) supported on aluminium copper oxide (Al_2CuO_4) nanosheets with abundant CuO/Al_2CuO_4 interfaces for achieving superior and selective ethylene production from electrochemical CO_2 conversion, synthesized by an economical co-precipitation and calcination approach. Impressively, the optimized catalyst (CuAl-**1**: CuO/Al_2CuO_4-23, where 23 denotes the total weight percent of Al to Cu) displays remarkable selectivity for ethylene (which is much higher than the as-synthesized bare CuO catalyst and electropolished polycrystalline Cu foils) and suppressed hydrogen evolution reaction (HER). Furthermore, using this CuAl-**1** catalyst in a flow-cell electrolyzer, we achieved C_2H_4 with a partial current density of 421 mA cm^{-2} in 1 M KOH, which is ~1.61-fold higher than the bare CuO catalyst. The results from operando electrochemical attenuated total reflection surface-enhanced infrared absorption spectroscopy (ATR-SEIRAS) revealed a higher CO content and more stabilized *CO intermediates on the CuAl-**1** compared to bare CuO during the CO_2RR, which results in an ultrahigh CO_2 to C_2H_4 selectivity. Our density functional theory (DFT) studies show that CO is more efficiently produced at the CuO site and then this CO is readily transferred to the Al_2CuO_4 site, where the Al_2CuO_4 surface provides a thermodynamic driving force to combine two adjacent CO for further electrochemical C–C steps to produce C_2H_4. Thus, we suggest that the presence of both CuO and Al_2CuO_4 surfaces gives rise to a synergistic effect and accelerates the CO_2RR to C_2H_4.

Results and discussion

Synthesis and structural characterization

The synthesis of CuAl-**1** involves a two-step process. First, the CuAl-**1** was prepared by co-precipitation of $Cu(NO_3)_3{\cdot}3H_2O$ and $Al(NO_3)_3{\cdot}9H_2O$ salts (the details synthesis method are provided in the Experimental section), and then subsequently calcined at 800 °C in a pure oxygen atmosphere for 5 h. To optimize the weight ratio (wt%) of Cu and Al in CuO/Al_2CuO_4-*x* (*x* denotes the wt% of Al to Cu) catalysts for high C_2H_4 selectivity, the salt weight ratio of $Cu(NO_3)_3{\cdot}3H_2O$ to $Al(NO_3)_3{\cdot}9H_2O$ was adjusted to 3.0 : 3.0 g, 3.0 : 1.0 g and 3.0 : 5.0 g to obtain CuO NPs on Al_2CuO_4 nanosheets with three different compositions (see Experimental section). For comparison, we also synthesized

 This journal is © The Royal Society of Chemistry 2022

Published on 22 March 2022. Downloaded by Ulsan National Institute of Science & Technology (UNIST) on 4/25/2022 10:19:47 AM.

pure CuO NPs without the support of Al_2CuO_4. The weight ratios of Cu and Al in the as-synthesized CuO/Al_2CuO_4-*x* catalysts were determined by inductively coupled plasma optical emission spectroscopy (ICP-OES). According to the ICP-OES results, the CuO/Al_2CuO_4-*x* with a wide range composition of Cu and Al can be prepared by adjusting the salt ratio of $Cu(NO_3)_2{\cdot}3H_2O$ to $Al(NO_3)_3{\cdot}9H_2O$ (Table S1, ESI†). Henceforth, the Cu and Al ratio in all the designed CuO/Al_2CuO_4-*x* catalysts are denoted by the composition ratios achieved from the ICP-OES analysis and for convenience, the catalysts are denoted as CuO/Al_2CuO_4-23 (CuAl-**1**), CuO/Al_2CuO_4-9 (CuAl-**2**), and CuO/Al_2CuO_4-32 (CuAl-**3**). Among the synthesized catalysts, CuO/Al_2CuO_4-23 (CuAl-**1**) has a higher selectivity toward C_2H_4 generation from the CO_2RR; therefore, this catalyst was selected for extensive characterizations and electrochemical measurements.

Transmission electron microscopy (TEM) was employed to examine the structural morphology of the CuO and Al_2CuO_4 in CuAl-**1**. The low magnification TEM image reveals that CuO NPs are well decorated on the ultrathin Al_2CuO_4 nanosheets (Fig. 1a). The high-resolution TEM (HRTEM) image shows that the NPs in CuAl-**1** are crystalline with the lattice fringes of 0.253 nm, which corresponds to the distance for the (111) plane of the monoclinic CuO crystal packing, whereas the lattice fringes of the nanosheet are 0.286 nm, corresponding to the (220) plane of the cubic Al_2CuO_4 crystal (Fig. S1, ESI†). In addition, the HRTEM image indicates that the CuO NPs are well contacted with the Al_2CuO_4 forming the CuO/Al_2CuO_4 interface. To examine the CuO/Al_2CuO_4 interface at the atomic scale arrangement, we used atomically resolved high angular annular dark field-scanning transmission electron microscopy (HAADF-STEM) analysis. The HAADF-STEM image taken from the orange and blue squares of Fig. 1b (left and Fig. S2 and S3, ESI†) reveals a clear interface between CuO and Al_2CuO_4 with a distinctly different atomic arrangement and crystal structures (Fig. 1b, right). The atomic arrangement in the Al_2CuO_4 nanosheet matches the spinel structure with the space group $Fd\bar{3}m$ (inset atomic model[35]), where the Cu^{2+} cations occupy the tetrahedral sites and Al^{3+} cations occupy the octahedral sites (Fig. 1c-left and Fig. S4, ESI†). The HAADF-STEM images with their corresponding line intensity profiles further confirm the distribution of Cu and Al elements in each atomic column (Fig. S4 and S5, ESI†). The inset atomic model in Fig. 1c (right) indicates that the arrangement of atoms in the CuO NPs matches that expected for the monoclinic lattice with the space

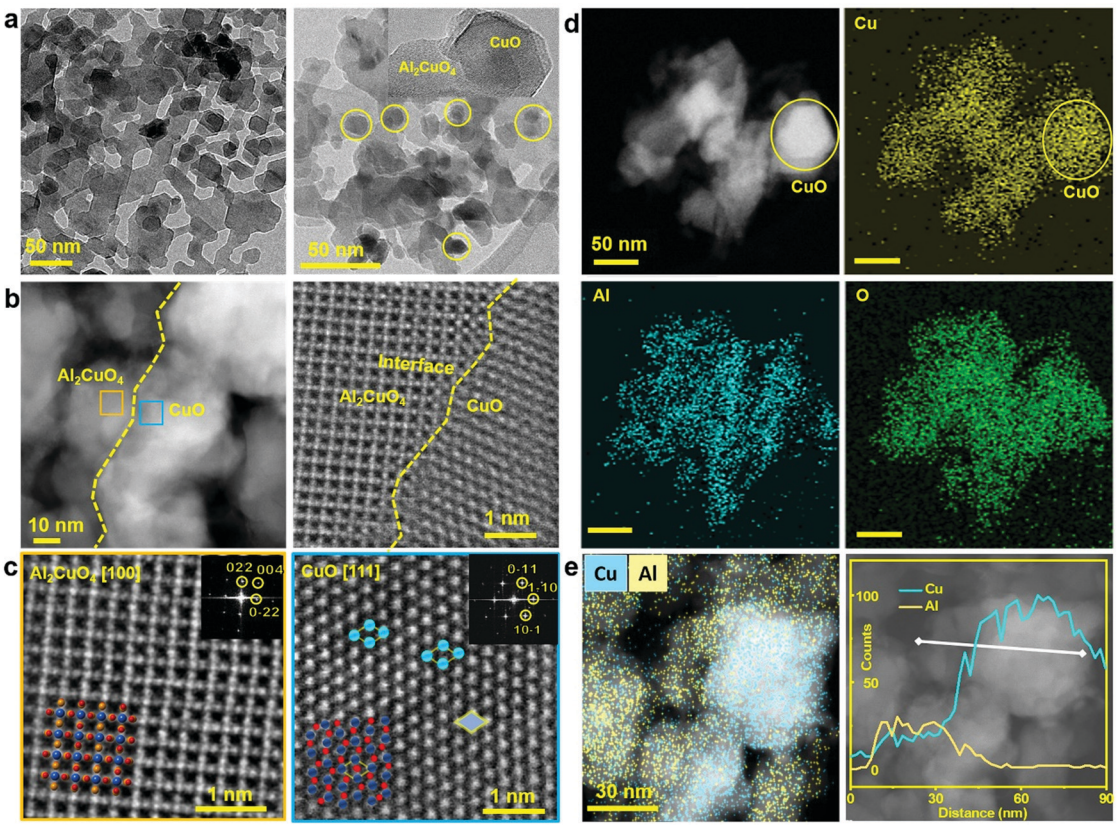

Fig. 1 Morphological and structural characterization of CuAl-**1**. (a) TEM images (in right side figure the yellow circles denote the CuO NPS). (b) HAADF-STEM images at the CuO/Al_2CuO_4 interface; low magnification STEM image (left) and atomic resolution STEM image of the CuO/Al_2CuO_4 interface (right). The right-side figure was taken from the interface between the orange and blue squared regions of the left side figure. (c) Magnified STEM images, FFT patterns and the corresponding ball and stick models for Al_2CuO_4 (left) and CuO (right). The insets on the corresponding lattice sites are the ball and stick models for the Al_2CuO_4 (left) and CuO (right); the blue, yellow and red balls in the inset models refer, respectively, to the atoms of Cu, Al and O. (d) HAADF-STEM image and their corresponding individual element maps of Cu, Al and O. The yellow circles (top) denote the CuO NPs. (e) HAADF-STEM image and their corresponding EDS mapping (left) and line-scan profiles (right).

Published on 22 March 2022. Downloaded by Ulsan National Institute of Science & Technology (UNIST) on 4/25/2022 10:19:47 AM.

group *C*2/*c* (Fig. S6, ESI†). The strain effect is often induced in an interface heterostructure crystal (due to the lattice mismatch of two adjacent phases)[36,37] when the two phases are epitaxially formed. The HAADF-STEM image of CuAl-**1** shows that CuO and Al_2CuO_4 do not have an epitaxial relationship (Fig S7, ESI†); therefore, the compressive or tensile strain was not observed when measuring the lattice spacing of Al_2CuO_4 (Fig S7a and b, ESI†). However, a careful examination of the CuO/Al_2CuO_4 interface reveals local lattice distortion in the CuO phase (marked as yellow lines in Fig S7a, ESI†) which is induced by adjacent interfacial defects but does not show any surface reconstruction at the CuO and Al_2CuO_4 edges (Fig S7c, ESI†). We also performed HAADF-STEM and the corresponding energy-dispersive spectroscopy (EDS) elemental mapping of both the nanosheets and NP area in CuAl-**1** (Fig. 1d), where the uniform distribution of Cu (yellow), Al (bluish-green) and O (green) is observed in the entire nanosheets decorated with CuO NPs on the surface (NPs contain Cu and O but no Al content; Cu: yellow; O: green). Fig. 1e is the overlay EDS mapping image (left) and the corresponding EDS-line scan at the CuO/Al_2CuO_4 interface (scanned by marked line in Fig. 1e, right), which further suggests that the NPs are pure Cu and nanosheets are a mixture of Cu and Al. The morphological differences in the CuAl-**1**, CuAl-**2**, and CuAl-**3** catalysts by the HAADF-STEM images and their corresponding EDS elemental mapping are provided in Fig. S8–S10 (ESI†). The HAADF-STEM images and EDS mapping confirmed that all three CuAl catalysts are composed of CuO and Al_2CuO_4 phases, but in different sizes and quantities (Fig S8, ESI†). The CuAl-**2** (9 wt% Al to Cu) has small contents of Al_2CuO_4, which is mainly covered with CuO NPs and therefore has fewer available interface sites of Al_2CuO_4 to CuO (Fig. S8d–f and S9, ESI†). On the other hand, CuAl-**3** (32 wt% Al to Cu) contains the largest population of Al_2CuO_4 sites and therefore has a small content of isolated CuO NPs (Fig. S8g–i and S10, ESI†). The TEM and EDS images of the as-synthesized pure CuO NPs without the support of Al_2CuO_4 are provided in Fig. S11 (ESI†).

To verify the existence of both CuO and Al_2CuO_4 in our designed catalysts, we performed high-resolution X-ray diffraction (HR-XRD) analysis of CuAl-**1** and other control catalysts (Fig. 2a and Fig. S12, ESI†). For better comparison, we also provide the HR-XRD spectra of the bare CuO catalyst (Fig. 2a). The XRD pattern of CuO displays the main dominant diffraction peaks at position 2θ of 32.52°, 35.49°, 38.689°, 48.66°, 58.25°, 61.52°, 66.15°, and 68.88°, corresponding respectively to the (110), (−111), (111), (−202), (202), (−113), (−311) and (220) planes of the monoclinic CuO crystal structure (JCPDS# 01-080-1916). In the XRD pattern of the CuAl-**1** catalyst, the diffraction peaks belonging to the monoclinic CuO crystal become weakened in favor of newly emerged peaks at 31.26°, 36.86°, 44.79°, and 55.62 that can be attributed respectively to (220), (311), (400) and (422) lattices of Al_2CuO_4 (JCPDS# 01-076-2295). We also observed from the XRD spectra that the peaks related to Al_2CuO_4 grew in intensity with increasing Al content, indicating changes in the ratio of CuO and Al_2CuO_4 in the CuAl-**1** to CuAl-**3** catalysts (Fig. S12, ESI†).

X-ray photoelectron spectroscopy (XPS) experiments were used to gain insight into the electronic interaction between

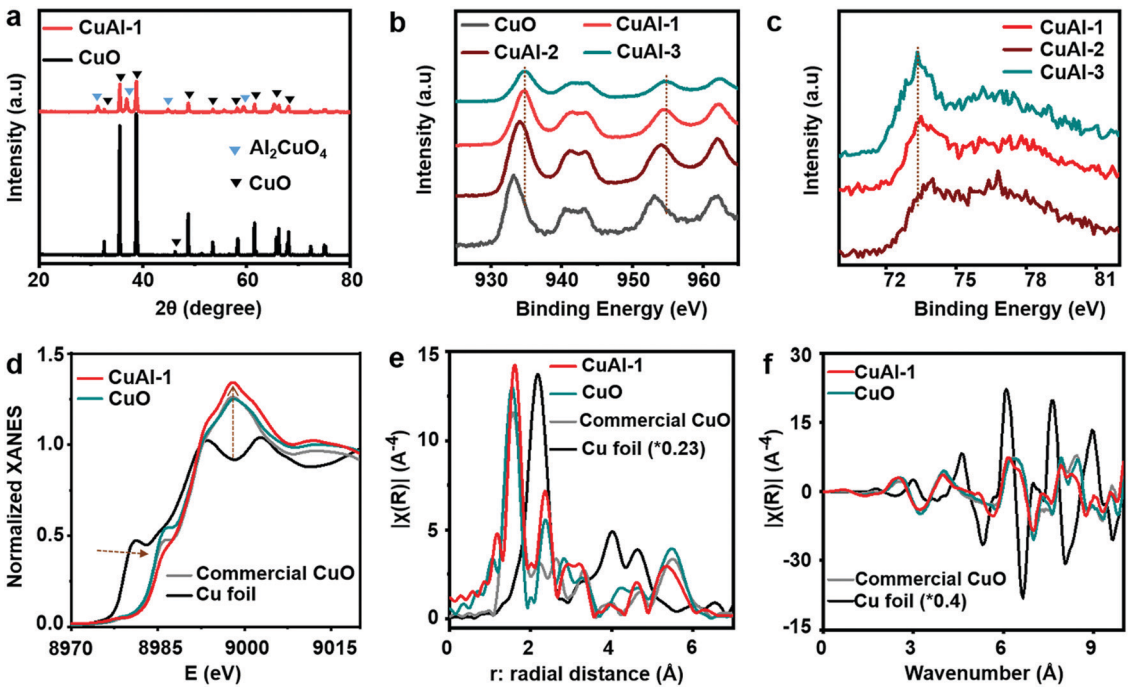

Fig. 2 Chemical and structural characterization. (a) XRD pattern of CuAl-**1** and CuO. (b and c) Comparison of the core level XPS spectra of Cu 2p and Al 2p between CuO and CuAl-**1** to CuAl-**3**. (d–f) X-ray absorption spectra for CuAl-**1**, CuO catalyst, commercial CuO powder and Cu foil; (d) XANES spectra in real space at the Cu K-edge; (e) FT-EXAFS spectra in *r*-space and (f) the k3χ oscillation signal in *k*-space.

 This journal is © The Royal Society of Chemistry 2022

Published on 22 March 2022. Downloaded by Ulsan National Institute of Science & Technology (UNIST) on 4/25/2022 10:19:47 AM.

Cu and Al as well as surface chemical states of each element in CuAl-**1**, CuO and other control catalysts. The core-level XPS spectra of Cu 2p obtained for CuAl-**1**, CuO and other control catalysts are shown in Fig. 2b. It can be seen that the Cu 2p peaks in CuAl-**1** are located at a higher energy side than the Cu 2p of CuO catalyst and this shift gradually increases with increasing Al content, which indicates the charge transfer from Cu to Al.[38] Similarly, we also observed a clear shift in the Al 2p peaks to the lower energy side with the increase in Cu content (Fig. 2c) which further suggests the energetically favourable charge transfer from Cu to Al in the CuO/Al_2CuO_4 system.[39] To further explore the valence state of each constituent element in the CuAl-**1** catalyst, we performed peak fitting of the Cu-2p, Al-2p/2s and O 1s spectra (Fig. S13, ESI†). The core-level XPS spectrum of Cu-2p shows pairs of peaks with similar spin-orbits at binding energies of 934.13/953.98 eV and 935.42/955.70 eV, which corresponds to Cu 2-p1/2, 3/2 spin-orbits of divalent Cu in CuAl-**1** (Fig. S13a, ESI†).[40] At the same time, the divalent oxidation state of Cu in CuAl-**1** is confirmed by strong charge transfer shake-up satellite peaks of the Cu ($2p_{3/2}$) and Cu ($2p_{1/2}$) at 941.06/943.70 and 958.91/962.16 eV, respectively (Fig. S13a, ESI†).[40] The core-level XPS spectrum of Al is deconvoluted into three peaks; the peaks located at binding energies of 73.64 eV and 78. 15 eV are assigned to the Al 2p levels of Al^{3+}, while the peak at a binding energy of 75.94 eV corresponds to Cu 3p photoelectrons (Fig. S13b, ESI†). We also check the XPS spectrum of Al in the 2s core-level region (in the high copper concentrations, one may acquire the Al spectra in both the Al-2p and Al 2s region) which shows two main peaks of Al^{3+} at binding energies of 117.99 and 118.71 eV (Fig. S13c, ESI†). The O-1s XPS spectrum shows two peaks at 530.10 and 531.29 eV, assigned to metal oxide species (Fig. S13d, ESI†).[41] The core-level XPS spectra of CuAl-2, CuAl-3 and CuO are provided in Fig. S14–S16 (ESI†).

The chemical state of Cu changed greatly from CuO to CuO/Al_2CuO_4; therefore, it is necessary to investigate local structural and electronic information about the Cu element. To gain deeper insight into the chemical state and coordinating environment of Cu in CuO and CuAl-**1** at an atomic scale, synchrotron X-ray absorption near-edge structure (XANES) and extended X-ray absorption fine structure (EXAFS) analysis were conducted. Fig. 2d presents the XANES profiles at the Cu K-edge of CuAl-**1** and bare CuO catalysts with Cu foil and commercial CuO as references. For Cu K-edge XANES, the energy positions of bare CuO are located beyond Cu foil and very close to commercial CuO powder, suggesting that the average oxidation state of Cu is nearly +2 in the bare CuO catalyst. In the case of CuAl-**1**, the energies of the Cu K-edges are positively shifted compared with those of the bare CuO catalyst and commercial CuO powder. In addition, the white-line peak intensity of the CuAl-**1** is higher than those of the synthesized CuO catalyst and commercial CuO powder. These results suggest that the overall charge of Cu in the CuAl-**1** is more positive than that of the CuO catalyst and commercial CuO powder, which contributes to the electron transfer from Cu to Al. Furthermore, the Cu K-edges from CuAl-**1** to CuAl-**3** gradually shift to the high-energy direction which agrees with the XPS data, suggesting that the average oxidation state of Cu increased with the increase of the Al amount from CuAl-**1** to CuAl-**3** (Fig. S17, ESI†). Fig. 2e illustrates the Fourier transform (FT) EXAFS spectra of CuAl-**1**, CuO and the references (Cu foil and commercial CuO powder). The (FT) EXAFS spectra of CuAl-**1** are similar to that of the CuO reference, which shows the first sharp dominant peak of Cu–O scattering at ~1.63 Å and the second peak of Cu–O–Cu coordination at ~2.3 Å, while there is no clear peak of Cu–Cu coordination compared with Cu foil (Fig. 2e). Furthermore, the $k3\chi$ (k) oscillation curve of CuAl-**1** and CuO at the Cu K-edge shows a similar trend in shape and oscillating frequency to that of the commercial CuO powder and is obviously different from that of Cu foil, inferring that the Cu in CuAl-**1** is of similar nature to CuO (Fig. 2f).

Electrochemical CO_2 conversion performance

The electrochemical CO_2RR performance of the CuAl-**1** was first evaluated in a gas-tight H-cell with a CO_2-saturated 0.1 M $KHCO_3$ electrolyte *via* the chronoamperometry measurements method for 60 min at an applied potential between −0.65 and −1.08 V with reference to the reversible hydrogen electrode (*vs.* RHE). Gaseous products were probed and quantified during the CO_2RR using online gas chromatography (GC) and liquid products were examined after completion of the electrochemical reaction *via* high-performance liquid chromatography (HPLC). For comparison, the CO_2RR activities of the electropolished Cu electrode, as-synthesized CuO and other control samples were also checked under the same testing conditions. The electrochemical experiment at each condition was performed at least three times and the mean values were used. As most of the CO_2RR products of our catalysts were in the gas phase with a small amount of liquid product (Fig. S18–S21, ESI†), in the main text we focused our discussions only on the gas-phase products. Fig. 3a–d reports the FE toward gas products for CuAl-**1**, CuO and the electropolished Cu electrode. For the CuAl-**1**, the production of C_2H_4 starts at a cathode potential of −0.75 V (FE_{C2H4} of 26.4%@−0.75 V) with an abundant amount of CO and H_2 gases (Fig. 3a). As more cathodic potential was applied, the production of CO and H_2 dramatically decreased while the FE for C_2H_4 production increased. At −0.99 V, the FE for C_2H_4 formation on CuAl-**1** reaches 79.4% ± 3, while those on CuO and the electropolished Cu electrode are only 51.28% ± 2 and 27.37% ± 2, respectively (Fig. 3a–d). Interestingly, in the potential window at which the FE for C_2H_4 formation is high, a small amount of CO was detected on the CuAl-**1** (Fig. 3a), while the CuO (Fig. 3b) and electropolished Cu electrode (Fig. 3c) show considerable formation of competitive CO or other C_1 products (CuO: FE_{CO} 7–20% and electropolished Cu electrode FE_{CO} 5–27%). This indicates that adsorbed CO, which is an intermediate for the formation of C_2 products (often generated along with ethylene), is strongly confined to the CuAl-**1** surface for a facilitated C–C coupling without desorbing it from the catalyst surface of CuO or the electropolished Cu electrode. The H_2 FE on the CuAl-**1** catalyst was also suppressed to ~11%, twice lower than that obtained from the CuO catalyst. To our knowledge and based on our data, CuAl-**1** is ranked as one

Published on 22 March 2022. Downloaded by Ulsan National Institute of Science & Technology (UNIST) on 4/25/2022 10:19:47 AM.

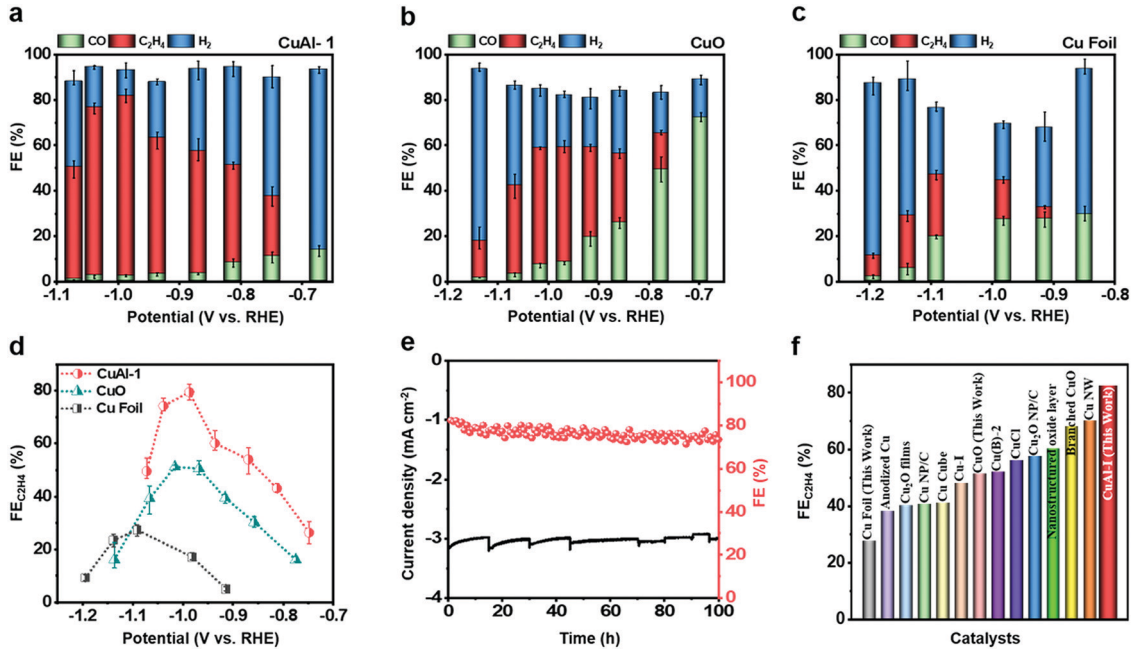

Fig. 3 Electrocatalytic CO_2RR of CuAl-**1**, CuO and electropolished polycrystalline Cu foil. (a–c) Product distributions and corresponding faradaic efficiencies produced by (a) CuAl-**1** (b) CuO and (c) electropolished polycrystalline Cu foil at different applied potentials in CO_2 saturated 0.1 M $KHCO_3$ electrolyte. (d) Comparison of ethylene faradaic efficiencies for CuAl-**1**, CuO and Cu foil at different applied potentials. All the error bars in (a–d) represent the standard deviation based on three independent measurements. (e) Stability test of CuAl-**1** at −0.99 V in CO_2 saturated 0.1 M $KHCO_3$ electrolyte. (f) Comparison of the ethylene faradaic efficiency of CuAl-**1** with previously reported state-of-the-art Cu-based catalysts (the details of (f) are provided in Table S4, ESI†).[17,18,20,23–26,30,32–34]

of the best selective catalysts among the top tier catalysts reported for the conversion of CO_2 to C_2H_4 (Fig. 3f and Fig. S18–S20 and Table S4, ESI†).

To investigate the effects of the Cu and Al weight ratio on the FE of C_2H_4, we compared the CO_2RR activity of the CuAl-**1** catalyst with CuAl-**2** (contains 9 wt% Al to Cu) and CuAl-**3** (contains 32 wt% Al to Cu). Interestingly, we found that all three (CuAl-**1** to CuAl-**3**) catalysts show higher selectivity for C_2H_4 formation than the bare CuO catalyst, suggesting that the Al_2CuO_4 surrounded CuO nanoparticles are more favourable sites for the C–C coupling than the pure CuO nanoparticles (Fig. S18 and S19, ESI†). Among the three CuAl-**1** to CuAl-**3** catalysts, CuAl-**1** shows a higher selectivity for the formation of C_2H_4 than CuAl-**2** and CuAl-**3** (Fig. S18 and S19, ESI†). From the XRD and HAADF-STEM analysis, we observed that the contents of the Al_2CuO_4 phase in CuAl-**1** to CuAl-**3** increase with increasing the Al amount in the catalysts. Based on XRD, HAADF-STEM analysis and electrochemical experiments, we conclude that the low C_2H_4 selectivity of the CuAl-**2** catalyst is likely due to the lower available interface sites of Al_2CuO_4 to CuO for the C–C coupling reactions, which is in agreement with the observed increase in FE of CO and formate on the CuAl-**2** (Fig. S18 and S19, ESI†). On the other hand, the decrease in C_2H_4 selectivity on the CuAl-**3** is explained by the fact that the sample with the largest population of Al_2CuO_4 sites may suffer from a reduced number of CuO sites, which cannot efficiently produce CO to increase the local CO concentration and surface coverage of *CO intermediates for the C–C coupling reactions, in agreement with the observed increase in the H_2 or C_1-product FEs at the expense of C_2H_4 (Fig. S18 and S19, ESI†). Thus, we suggest that both Al_2CuO_4 and CuO play an important role in enhancing the C–C coupling to C_2H_4; therefore, the optimal ratios of Al_2CuO_4 and CuO in CuAl-**1** synergistically accelerated the CO_2-to-C_2H_4 performance.

To assess the long-term stability of CuAl-**1**, a chronoamperometry test was performed at −0.99 V for 100 h. The CuAl-**1** shows an almost stable constant current density with a little decrease in C_2H_4 FE in the course of 100 h (Fig. 3e). The catalyst after the stability test was characterized by XRD analysis, which shows almost identical spectra to those before the test (Fig. S22, ESI†), indicating the excellent structural and chemical stability of CuAl-**1**. The ICP-OES analysis of the catalyst and electrolyte before and after the durability test also supports the high electrocatalytic and chemical/structural stability of the CuAl-**1** catalyst for the long-term electrocatalysis of the CO_2RR (Fig. S23, ESI†).

To demonstrate the potential scalability of CuAl-**1** for industrially relevant C_2H_4 production, we further tested the CO_2RR on CuAl-**1** and CuO electrodes in a flow-cell system. First, we deposited the catalyst ink on a carbon gas diffusion electrode (GDE) *via* a spray-coating method; the other details are provided in the (ESI†). Afterwards, the CO_2RR activity was measured at current densities between 100 and 1000 mA cm^{-2} (potential values were between −0.985 and −2.42 V_{RHE} for CuAl-**1**) *via* chronopotentiometry test (Fig. S24, ESI†), where 1 M KOH electrolyte was continuously introduced into the cell.

This journal is © The Royal Society of Chemistry 2022

Published on 22 March 2022. Downloaded by Ulsan National Institute of Science & Technology (UNIST) on 4/25/2022 10:19:47 AM.

We achieved 70.1 ± 2% FE for C_2H_4 at a current density of 600 mA cm^{-2} (−2.031 V_{RHE}) when CuAl-**1** was used as an electrode, while the maximum FE for C_2H_4 on our synthesized CuO and commercial CuO electrodes was only 52.3 ± 2% and 18.2 ± 2%, respectively (Fig. S25, ESI†). Moreover, the partial current density of CuAl-**1** for C_2H_4 is 421 mA cm^{-2}, which is ~1.61-fold higher than that of CuO and is far better than the commercial CuO catalyst (Fig. S26, ESI†). The details of FE and partial current densities for C_2H_4 and other gases/liquid products at different applied current density/potential values, KOH concentration and pH values on CuAl-**1**, our synthesized bare CuO and commercial CuO electrodes in a flow-cell system are provided in Fig. S25–S28 (ESI†). The electrocatalytic CO_2RR performance of CuAl-**1** in the flow cell with CO_2 saturated 0.1 M $KHCO_3$ electrolyte in comparison with a H-cell are provided in Fig. S29, (ESI†).

To gain insight into the intermediate adsorption and C–C coupling on CuAl-**1** and CuO catalysts, we performed time-resolved attenuated total reflection-surface enhanced infrared absorption spectroscopy (ATR-SEIRAS) during the real-time CO_2RR conditions using multiple chronoamperometric scans (Fig. S31, ESI†). In Fig. 4a (CuO) and 4b (CuAl-**1**), the C≡O stretching band of *CO (2060 cm^{-1} for CuO and 2068 cm^{-1} for CuAl-**1** at −0.56 V) and the C=O stretching band of *OCCO (1545 cm^{-1} for CuO and 1560 cm^{-1} for CuAl-**1**)[42] were observed with increasing applied potential. To find the origin of the band near 1560 cm^{-1} (*OCCO), we performed an isotope labelling experiment on CuAl-**1** using a $^{13}CO_2$ saturated 0.1 M $KHCO_3$

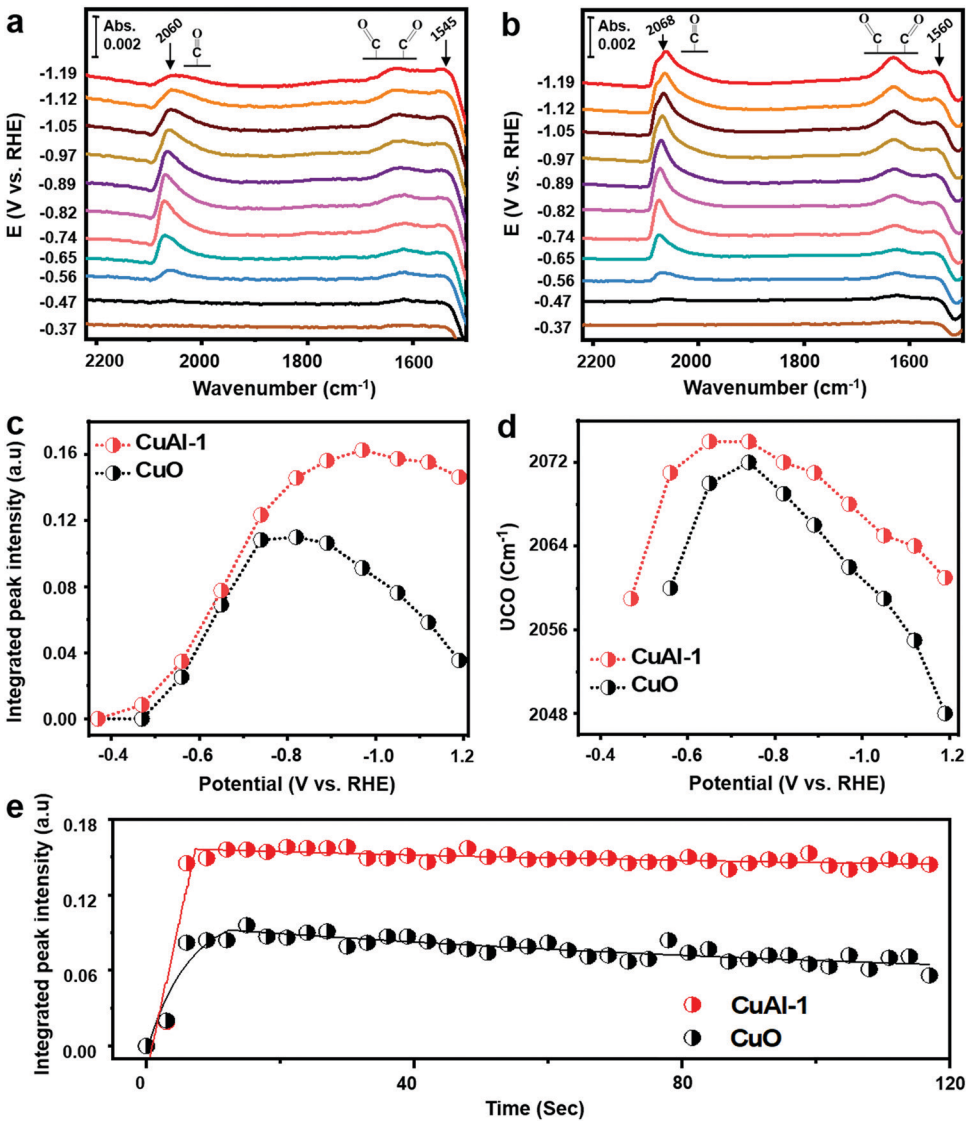

Fig. 4 *In situ* ATR-SEIRAS analysis of CuAl-**1** and CuO. (a and b) Potential-dependent IR spectra of (a) CuO and (b) CuAl-**1** during chronoamperometric scans from −0.37 V to −1.19 V. (c) The integrated peak intensities and (d) vibrational frequency of *CO (2040–2080 cm^{-1}) on CuO and CuAl-**1**. (e) The integrated peak intensities of *CO band spectra of CuO and CuAl-**1** during *in situ* ATR-SEIRAS measurement. The spectra were collected at −0.97 V for 120 s. The red and black balls in (e) denote the data and lines represent the fitting. Experimental conditions: CO_2 saturated 0.1 M $KHCO_3$ D_2O electrolyte with the baseline spectrum at −0.28 V. The peak positions were determined by the maximum intensity of the CO bands.

Published on 22 March 2022. Downloaded by Ulsan National Institute of Science & Technology (UNIST) on 4/25/2022 10:19:47 AM.

solution, which showed a red/shift of about 60 cm^{-1}, confirming that the band near 1560 cm^{-1} originated entirely from the electrochemical CO_2RR (Fig. S30b, ESI†). *OCCO can be generated from the CO dimerization while the C═O stretching bands of the *CHO band as a key intermediate for CH_4 formation were absent in both catalysts.[42] These results are consistent with the product distribution (Fig. 3) obtained for each catalyst. For in-depth monitoring of the potential-dependent behavior of *CO, their integrated peak intensities were plotted against the applied potentials (Fig. 4c). On CuO, *CO appears simultaneously at −0.56 V, which is close to the onset potential (Fig. S18 ESI†). The band gradually increases until −0.82 V and then decreases at more negative potentials. This implies the accumulation of *CO intermediates under insufficient overpotentials and further transforming into gas-phase CO or more reduced species (*e.g.* C_2H_4) at high overpotentials. In the case of CuAl-**1**, the integrated peak intensity of *CO was saturated above −0.82 V, indicating that *CO is continuously replenished from the CO_2RR although *CO is significantly consumed for the production of C_2H_4. Fig. 3d shows the vibrational frequency of CO (νCO) during the cathodic chronoamperometric scan. Before the onset potential (−0.47 V to −0.65 V), νCO of both CuO and CuAl-**1** show a blue shift as the potential is lowered to the negative region. At such potentials, adsorption has taken place, but the CO_2RR has not yet occurred, and the observed blue-shift of νCO results from the dipole interaction effect between the covered *CO species as the π-back bonding from the metal decreases. This indicates that the CO coverage on both CuO and CuAl-**1** is dense enough to cause the dipole interaction effect. At potentials below −0.74 V, νCO decreases linearly with the lowering potential (Φ) due to the Stark effect.[43,44] The slope of the shift ($d\nu/d\Phi$) is approximately 40 cm^{-1} V^{-1} for CuO, in accordance with previous reports.[45,46] In the case of CuAl-**1**, the slope of the shift is lower than that of CuO (approximately 30 cm^{-1} V^{-1}), which indicates the stronger CO bound on the Cu surface. This is probably because the partial positive charges on the Cu surface in CuAl-**1** play an important role in reducing the σ-interaction (repulsive) between the CO and Cu surfaces.[47] The relatively improved attractive π-interaction (caused by the decreased repulsive effect of the σ-interaction) in CuAl-**1** signifies that CO is more strongly adsorbed to its surface relative to CuO, which results in its higher wavenumber.[48,49] To further investigate the kinetic behaviors of *CO intermediates during the CO_2RR, time-resolved IR analysis on the time scale of seconds was conducted at constant bias potentials (Fig. 4e and Fig. S32, ESI†). At −0.97 V (the potential at which the C_2 product was most produced), we observed clear peak intensities of the *CO band on both catalysts. Fig. 4e shows the higher integrated intensities (*ca.* 2 times) of the *CO band in CuAl-**1** and its slower decay kinetics, indicating that *CO is more densely covered and promptly replenished in CuAl-**1** relative to CuO.

We also performed X-ray absorption spectroscopy (XAS) measurements at the Cu K-edge in CuAl-**1** and CuO to investigate the Cu chemical state of the catalysts during and after the CO_2RR. We observed a profound change in the XANES and (FT) EXAFS spectra of the CuO catalyst after the chronoamperometry test (Fig S33a, ESI†). The Cu K-edge in the XANES spectra of the CuO catalyst after the reaction shows a prominent shift towards lower energy and its pre-edge and white-line peaks are nearly identical to the spectrum of a metallic Cu foil (Fig. S33a, ESI†). In the (FT) EXAFS spectra of the CuO catalyst, the peak related to the Cu–O bond decreased to a minimum and a new strong peak appeared at 2.17 Å, corresponding to the Cu–Cu bonds in metallic Cu (Fig. S33b, ESI†). At the same time, the $k3\chi$ (k) oscillation curve of CuO after the chronoamperometry test shows a similar shape in oscillating frequency to that of the metallic Cu foil (Fig. S33c, ESI†). For CuAl-**1**, we monitored the chemical state of Cu under real-time CO_2RR operating conditions in the catalytic state and after the chronoamperometry test. Fig. S34a and b (ESI†) show the *in situ* XANES and (FT) EXAFS spectra of the CuAl-**1** catalyst recorded approximately every 20 min under chronoamperometric conditions, where the electrode was biased at different applied potentials (V_{RHE}) from the open-circuit voltage (OCV) down to −1.05 V. Notably, the XANES spectra of CuAl-**1** show almost completely overlapped pre-edge and white-line peaks under CO_2RR operation from −0.75 to −0.85 V and are nearly identical to the OCV pattern. We only observed a slight band edge shift to lower energy in the XANES spectra of CuAl-**1** when the CO_2RR was operated in the highly reductive environment from −0.95 to −1.05 V, suggesting a partial reduction of the CuO center. Similarly, the (FT) EXAFS spectra of CuAl-**1** show an almost identical radial position for the Cu–O bond distance from OCV to −0.85 V and a slight shift towards a lower radial distance at more negative potentials of −0.95 to −1.05 V due to partial reduction of Cu ions. Consistent results were obtained when we compared the XANES and (FT) EXAFS spectra of CuAl-**1** after the chronoamperometry test (operated under the best performing condition) with the pristine electrode (Fig. S35, ESI†). The XANES and (FT) EXAFS spectra of the CuAl-**1** after the chronoamperometry test show only a little shift towards the lower energy and radial distance compared to the pristine electrode (Fig. S35a and b, ESI†). At the same time, the $k3\chi$ (k) oscillation curve of CuAl-**1** after the reduction reactions shows a similar shape in oscillating frequency to that of the pristine electrode (Fig. S34c and S35c, ESI†). Thus, the XAS results demonstrate that Cu in the CuAl-**1** catalyst shows almost a stable positive oxidation state during the CO_2RR reaction and the C_2H_4 selectivity is associated with the oxidized copper rather than the existence of metallic state Cu.

Density functional investigation on the catalytic mechanism

To understand the origin of the high ethylene selectivity of the CuAl-**1** catalyst, density functional theory (DFT) calculations were performed. Among the (004), (220), and (111) surfaces of Al_2CuO_4, where the (004) and (220) surfaces were observed from STEM images (Fig. 1c and Fig. S4, S5, ESI†), our DFT calculations found that the (004) surface has the lowest surface energy as well as the strongest CO binding strength (Table S2, ESI†). On the other hand, previous studies have shown that the most stable low-index surface of CuO is the (111) surface.[50,51] Thus, we chose an Al_2CuO_4(004) surface slab and CuO(111) surface slab as our atomic models for the catalytic active sites (Fig. S36, ESI†).

 This journal is © The Royal Society of Chemistry 2022

Published on 22 March 2022. Downloaded by Ulsan National Institute of Science & Technology (UNIST) on 4/25/2022 10:19:47 AM.

The DFT energies for the CO_2 reduction to CO (Fig. 5a) show that the formation of *COOH on Al_2CuO_4 (1.04 eV) required more energy by a value of 0.22 eV than that of CuO (0.82 eV), inferring a better catalytic conversion of CO_2 to CO on the CuO surface. Furthermore, the binding energy of CO on Al_2CuO_4 is greater by a value of 0.15 eV than that of CuO, indicating that Al_2CuO_4 helps to prevent CO desorption from the catalyst surface and therefore leads to an increased surface coverage of CO for the further C–C coupling steps, which is consistent with the results obtained from the ATR-SEIRAS (Fig. 4).

We then investigated the energies for the coupling of two *CO molecules, which is known as the primarily determining step for the formation efficiency of C_2 products.[52–54] Fig. 5b shows that the binding energy of two *CO molecules on Al_2CuO_4 (0.75 eV) is lower by a value of 0.28 eV than that of CuO (1.03 eV). Interestingly, we find that although two CO are bound as a chemical form of *OCCO on the CuO surface where the C–C bond has already been coupled, the Al_2CuO_4 can provide a single binding site of surface Cu atom where two CO molecules can separately bind without incurring a direct C–C bond formation. We thus investigate further reduction steps including the C–C coupling step (Fig. 5c), which demonstrates favorable energies for the formation of ethylene under the low threshold potential of −0.62 V.

Fig. 5d shows the binding mode of two CO molecules to the Cu surface atom of Al_2CuO_4, where the charge difference map is also displayed. We find a tetrahedral geometry of Cu, of which smaller d-orbital splitting compared to the square planar geometry is conceived to offer a stronger binding of CO molecules. In addition, the charge difference map shows an accumulation of charge in the region between two C atoms (Fig. 5d), which can help in the formation of the C–C bond in the subsequent reaction step.

Thus, we suggest the following mechanism for the CO_2RR to C_2H_4 on the CuAl-**1** catalyst. First, CO is more efficiently produced at the CuO domain, where the *COOH is not only stable but also the CO desorption is favorable. Next, CO is transferred to the Al_2CuO_4 domain, which provides a thermodynamic driving force for CO binding. When two CO molecules are accumulated at the same active site of Cu, further electrochemical steps favourably occur to produce ethylene at the Al_2CuO_4 domain. Thus, for enhanced activity, it is important to maximize the interfacial regions where CO can be easily transferred, which supports the experimental finding of a synergistic effect between CuO and Al_2CuO_4. Moreover, the hydrogen binding energy (HBE) of Al_2CuO_4 (which is 0.97 eV) is greater than the HBE of CuO (which is 0.63 eV), supporting the suppressed HER of the CuAl-**1** catalyst (Table S3, ESI†). It is of note that both catalytic surfaces of Al_2CuO_4 and CuO locate at the weak binding leg of the activity volcano with the positive values of HBE.[55]

Our combined experimental, ATR-SEIRAS and theoretical studies have rationalized stronger CO adsorption on CuAl-**1**,

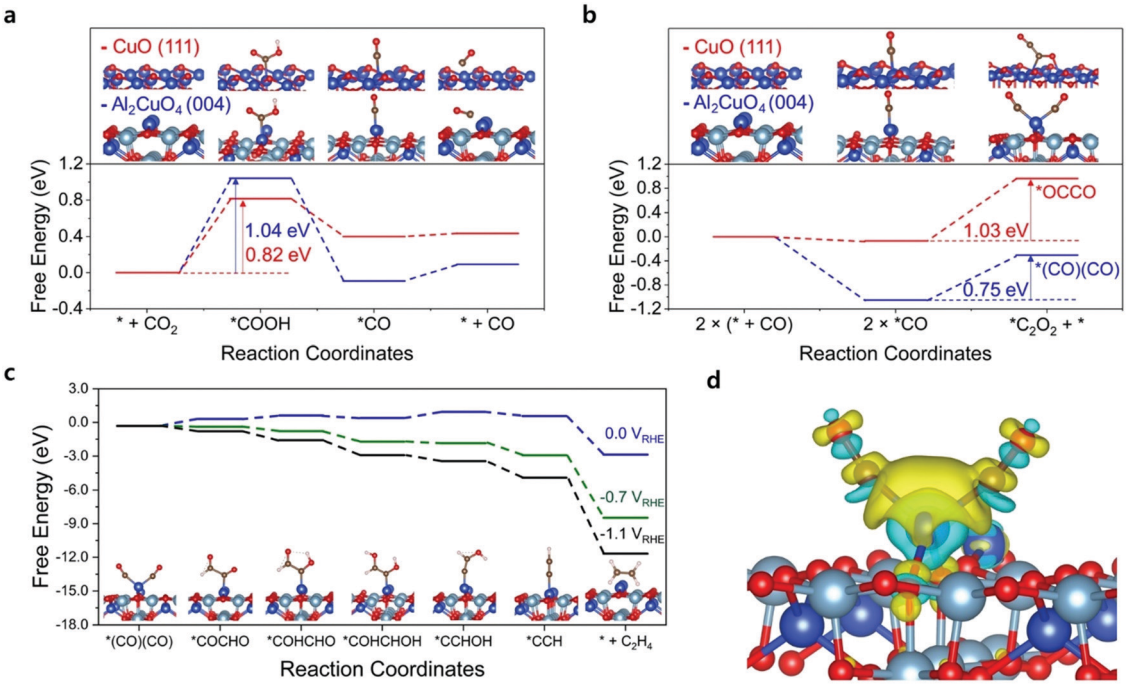

Fig. 5 DFT results of Al_2CuO_4 and CuO. (a) Free energy diagram of CO formation from CO_2 on the (004) facet of Al_2CuO_4 (blue) and (111) facet of CuO (red) at 0 V_{RHE}. The DFT-optimized structure for each step is shown in the inset. (b) Free energy diagram of two CO binding to the (004) facet of Al_2CuO_4 (blue) and (111) facet of CuO (red) at 0 V_{RHE}. The DFT-optimized structure for each step is in the inset. (c) Free energy diagram of ethylene formation after two CO binding on the (004) facet of Al_2CuO_4 at various potential conditions of 0 V_{RHE} (blue), −0.7 V_{RHE} (green), and −1.1 V_{RHE} (black). Insets show DFT-optimized structures. (d) Binding mode of two CO molecules to the Cu atom of the Al_2CuO_4 surface, where the charge difference map is also displayed. The charge accumulation and depletion are shown in yellow and cyan, respectively, at a ±0.005 e $Å^{-3}$ isosurface level. Al, Cu, O, C are represented as sky blue, blue, red, and brown color, respectively.

Published on 22 March 2022. Downloaded by Ulsan National Institute of Science & Technology (UNIST) on 4/25/2022 10:19:47 AM.

which not only prevents CO desorption from the catalyst surface but also increases and stabilizes the surface coverages of *CO intermediates for better C–C coupling toward the C_2 products. To further explore the catalytic behavior of CuAl-**1** with an increased local CO concentration, we conducted the electroreduction of CO (CORR) on CuAl-**1** in the flow cells using KOH as the electrolyte and the results are compared to those obtained from the as-synthesized CuO and commercial CuO samples (Fig. S37, ESI†). Interestingly, the CuAl-**1** achieved 35% selectivity for C_2H_5OH and 83% selectivity for the overall C_2 products (48% for C_2H_4 and 35% for C_2H_5OH) which is much higher than the as-synthesized CuO (44% for C_2H_4 and 10% for C_2H_5OH) and commercial CuO (30% for C_2H_4 and 8% for C_2H_5OH). The CORR results suggest that at local CO enrichment, it is likely that higher coverages of *CO intermediate have been induced on the CuAl-**1** surface for C–C coupling, leading to an increase in the formation of C_2H_5OH at the expense of C_2H_4.

Conclusions

To conclude, we have developed a CuO/Al_2CuO_4-23 catalyst for selective CO_2 electrochemical reduction to C_2H_4. This catalyst achieves ultrahigh activity and selectivity for C_2H_4 and high catalytic and material stability during the 100 h continuous CO_2RR chronoamperometry test in an H-cell system. When this catalyst is used in a flow-cell electrolyzer system, we achieve an exceptionally higher partial current density of 421 mA cm^{-2} without compromising the ethylene selectivity, which is ~1.61-fold greater than that of the bare CuO catalyst. The *in situ* XAS measurements revealed that the positive oxidation state of Cu in CuAl-**1** is well-retained during the CO_2RR and the high C_2H_4 selectivity of the catalyst is related to the oxidized copper rather than metallic state Cu. Using operando ATR-SEIRAS and DFT calculations, we reveal that the intriguing geometric/electronic structure of CuO and Al_2CuO_4 in CuAl-**1** enhances the local CO production, increases and stabilizes the *CO intermediates and decreases the HER kinetics relative to CuO alone and therefore, leads to greatly improved C_2H_4 selectivity.

Methods

Synthesis of the catalysts

The catalysts from CuAl-**1** to CuAl-**3** were synthesized by coprecipitation and calcination methods using different weight ratios of $Cu(NO_3)_2{\cdot}3H_2O$ to $Al(NO_3)_3{\cdot}9H_2O$ with 3.0 g of $(NH_4)_2CO_3$ as starting precursors. The precursor weight ratios of $Cu(NO_3)_2{\cdot}3H_2O$: $Al(NO_3)_3{\cdot}9H_2O$ for CuAl-**1**, CuAl-**2** and CuAl-**3** were 3.0 : 3.0 g, 3.0 : 1.0 g and 3.0 : 5.0 g, respectively. During the synthesis process, the required ratio of $Cu(NO_3)_2{\cdot}3H_2O$: $Al(NO_3)_3{\cdot}9H_2O$ was dissolved in 70 mL of DI water by sonication. Separately, 3 g of $(NH_4)_2CO_3$ was dissolved in another 70 mL of DI water. The two solutions were combined in 40 mL of hot DI water at 50 °C under vigorous stirring for 4 h and then aged for a further 3 h in static conditions. The resulting solid mixture was recovered by vacuum filtration, washed with DI water/ethanol, dried overnight at 70 °C and then ground thoroughly. The ground powder was finally calcined at 800 °C for 5 h with a temperature ramping rate of 3 °C min^{-1} under flowing oxygen gas (100 sccm). The synthesis procedure for the CuO catalyst was the same as for CuAl-**1** to CuAl-**3** except without the use of the $Al(NO_3)_3{\cdot}9H_2O$ salt.

Electrochemical measurements

The electrochemical experiments were performed on a VSP-modular 2 Channels Potentiostat/Galvanostat/EIS (Bio-Logic Science Instruments) at room temperature. The electrochemical measurements were first conducted in a two-compartment H-type cell with a three-electrode system using 0.1 M $KHCO_3$ solution as both catholyte and anolyte. The glassy carbon electrode (GCE, geometric area of 6.25 cm^2), Ag/AgCl electrode (saturated KCl) and Pt foil were used as the working, reference and counter electrodes, respectively. For working electrode preparation, 10 mg powder of each catalyst with 40 μL of 5 wt% Nafion solution were homogeneously dispersed in 1000 μL of ethanol by ultrasonication, and then 300 μL of the catalyst ink was dropped onto the GCE (0.6 mg cm^{-2}). The ink on the GCE was then vacuum dried to obtain the working electrode for the subsequent electrochemical tests. The reference and working electrodes were placed in the cathode part, while the Pt foil was placed in the anode part, which was separated by a selemion anion exchange membrane for avoiding the mixing of cathode and anode products or the re-oxidation of CO_2RR products. Each chamber of the H-type cell contains 3 mL of electrolyte and the electrolyte in the cathode part was bubbled with high purity CO_2 gas for 20 min to form a CO_2 saturated solution and the flow rate (5 sccm, adjusted by a flow meter) was maintained during the electrochemical measurements. Note: at neutral pH and low current density the CO_2 conversion rate is low; therefore, the outlet gas flow is very little different from the inlet gas flow,[56] however, for greater accuracy, we use the outlet gas flow for faradaic efficiency calculations. The electrochemical CO_2RR performance for each catalyst was evaluated *via* the chronoamperometry measurements method for 60 min at different applied potentials from −0.65 V down to −1.08 V. All potentials used in this work were referenced to the RHE by adding a value of (0.196 + 0.059 × pH) V and corrected manually for iR-compensation. The detailed procedure for the faradaic efficiency calculations is provided in the Supplementary Information.

Product analysis

The gaseous products were identified and quantified in real-time from the cathodic part of the CO_2RR reactor by online gas chromatography (GC, model iGC 7200A) equipped with flame ionization detectors (FIDs for carbon product detection) and a thermal conductivity detector (TCD for H_2 detection). The gas products from the CO_2RR reactor were injected into the GC at regular intervals of 20 min during continuous 1 h chronoamperometry measurements. The actual amounts of each gas (H_2, CO and hydrocarbons) produced during the chronoamperometric test were calculated from the peak area of the GC

 This journal is © The Royal Society of Chemistry 2022

Published on 22 March 2022. Downloaded by Ulsan National Institute of Science & Technology (UNIST) on 4/25/2022 10:19:47 AM.

spectrum with conversion factors based on calibration of standard gases (Fig. S21, ESI†). The liquid products were analyzed using high-performance liquid chromatography (HPLC, 1260 Infinity II, Agilent Technologies) equipped with a NUCLEOGEL SUGAR 810 column and a refractive index detector and 5 mM sulfuric acid was used as the eluent.

DFT simulation

Spin-polarized density functional theory (DFT) calculations were performed using the Vienna *ab initio* Simulation Package (VASP) 5.4.4.[57] The projector-augmented pseudopotential and Perdew–Burke–Ernzerhof (PBE) exchange–correlation functional were used.[58,59] The kinetic energy cutoff of the plane-wave basis was set to 520 eV. The method of Methfessel–Paxton (MP) was used with a smearing width of 0.20 eV.[60] To sample the reciprocal space, a $(3 \times 3 \times 1)$ Γ-centered k-point grid was used. Along the surface normal direction, an additional $\sim$17 Å vacuum region was included, and a dipole correction was applied to exclude the electrostatic interactions between periodic surface images. During the geometry optimizations, the top layer of the slab model, as well as the adsorbate, was fully relaxed while the bottom layer was fixed. The convergence criterion was 1×10^{-4} eV for the self-consistent-field (SCF) iterations, and 1×10^{-3} eV for the geometry optimization. The implicit solvation method was used to include the solvation effects.[61] The free energy quantities were calculated as $\Delta G = \Delta E_{\mathrm{SCF}} + \Delta \mathrm{ZPE} - T\Delta S + \int_0^T C_{\mathrm{v}} \mathrm{d}t$, where E_{SCF} is the DFT SCF energy, and ZPE is the zero-point energy. For the gas molecules, rotation and translation were also considered in addition to vibration to calculate the free energy. Vibrational free energy quantities were calculated by diagonalizing a partial Hessian of the adsorbate molecule. During the calculation of vibration frequencies, the convergence criteria were set to 1×10^{-6} eV and 1×10^{-5} eV for the SCF iteration and geometry optimization, respectively. The atomic structures and charge difference map were displayed using VESTA v3.4.4.[62]

Author contributions

S. S. planned the experiment, electrochemical measurements and analyzed the data. S.S. and H. L. performed the catalysts synthesis and physical/chemical characterizations including the TEM and XAFS analysis. H. L. performed the electrochemical measurements and arranged the corresponding figures with support of H. C. and T. K. A. Y. and Z. L. performed the HAADF-STEM analysis. S. P. and W. K. performed *in situ* ATR-SEIRAS measurements. M. M. K. and H. K. performed the theoretical calculations. Y.-J. K. and H.-S. O. performed *in situ* XAS measurement. Y. K. supervised the project.

Conflicts of interest

There are no conflicts to declare.

Acknowledgements

This research was supported by the Basic Science Research Program of the National Research Foundation of Korea (NRF-2021R1A2C2007823), Carbon to X Project (NRF 2020M3H-7A1098231) funded by the Ministry of Science and ICT, Republic of Korea, and the Ulsan National Institute of Science and Technology (Project No. 1.210102.01). S. S. acknowledges the support from the Basic Science Research Program through the National Research Foundation of Korea (NRF-2021R1I1A-1A01059499) funded by the Ministry of Education. Z. L. acknowledges the support from the Institute for Basic Science (IBS-R019-D1). S. P and W. K. acknowledge the support from the National Research Foundation of Korea (NRF) grant funded by the Korea government (MSIT) (No. NRF-2021R1A5A1084921). The EXAFS experiments were performed in the Pohang Accelerator Lab (PAL), at the 6D UNIST-PAL beamline.

References

1 D. Gao, R. M. Arán-Ais, H. S. Jeon and B. Roldan Cuenya, *Nat. Catal.*, 2019, **2**, 198–210.
2 M. Zhong, K. Tran, Y. Min, C. Wang, Z. Wang, C.-T. Dinh, P. De Luna, Z. Yu, A. S. Rasouli, P. Brodersen, S. Sun, O. Voznyy, C.-S. Tan, M. Askerka, F. Che, M. Liu, A. Seifitokaldani, Y. Pang, S.-C. Lo, A. Ip, Z. Ulissi and E. H. Sargent, *Nature*, 2020, **581**, 178–183.
3 S. Sultan, J. N. Tiwari, A. N. Singh, S. Zhumagali, M. Ha, C. W. Myung, P. Thangavel and K. S. Kim, *Adv. Energy Mater.*, 2019, **9**, 1900624.
4 D. A. Salvatore, C. M. Gabardo, A. Reyes, C. P. O'Brien, S. Holdcroft, P. Pintauro, B. Bahar, M. Hickner, C. Bae, D. Sinton, E. H. Sargent and C. P. Berlinguette, *Nat. Energy*, 2021, **6**, 339–348.
5 P. D. Luna, C. Hahn, D. Higgins, S. A. Jaffer, T. F. Jaramillo and E. H. Sargent, *Science*, 2019, **364**, eaav3506.
6 Y. Chen, A. Vise, W. E. Klein, F. C. Cetinbas, D. J. Myers, W. A. Smith, T. G. Deutsch and K. C. Neyerlin, *ACS Energy Lett.*, 2020, **5**, 1825–1833.
7 J. Gu, C.-S. Hsu, L. Bai, H. M. Chen and X. Hu, *Science*, 2019, **364**, 1091–1094.
8 T. Zheng, K. Jiang, N. Ta, Y. Hu, J. Zeng, J. Liu and H. Wang, *Joule*, 2019, **3**, 265–278.
9 F. Pan and Y. Yang, *Energy Environ. Sci.*, 2020, **13**, 2275–2309.
10 J. Lim, P. W. Kang, S. S. Jeon and H. Lee, *J. Mater. Chem. A*, 2020, **8**, 9032–9038.
11 P. Ding, H. Zhao, T. Li, Y. Luo, G. Fan, G. Chen, S. Gao, X. Shi, S. Lu and X. Sun, *J. Mater. Chem. A*, 2020, **8**, 21947–21960.
12 L. Han, S. Song, M. Liu, S. Yao, Z. Liang, H. Cheng, Z. Ren, W. Liu, R. Lin, G. Qi, X. Liu, Q. Wu, J. Luo and H. L. Xin, *J. Am. Chem. Soc.*, 2020, **142**, 12563–12567.
13 R. Zhao, P. Ding, P. Wei, L. Zhang, Q. Liu, Y. Luo, T. Li, S. Lu, X. Shi, S. Gao, A. M. Asiri, Z. Wang and X. Sun, *Adv. Funct. Mater.*, 2021, **31**, 2009449.
14 D. Yang, Q. Zhu, C. Chen, H. Liu, Z. Liu, Z. Zhao, X. Zhang, S. Liu and B. Han, *Nat. Commun.*, 2019, **10**, 677.

Published on 22 March 2022. Downloaded by Ulsan National Institute of Science & Technology (UNIST) on 4/25/2022 10:19:47 AM.

15 R. Daiyan, X. Lu, Y. H. Ng and R. Amal, *ChemSusChem*, 2017, **10**, 4342–4358.
16 L. Ji, L. Li, X. Ji, Y. Zhang, S. Mou, T. Wu, Q. Liu, B. Li, X. Zhu, Y. Luo, X. Shi, A. M. Asiri and X. Sun, *Angew. Chem., Int. Ed.*, 2020, **59**, 758–762.
17 H. Jung, S. Y. Lee, C. W. Lee, M. K. Cho, D. H. Won, C. Kim, H.-S. Oh, B. K. Min and Y. J. Hwang, *J. Am. Chem. Soc.*, 2019, **141**, 4624–4633.
18 C. Choi, S. Kwon, T. Cheng, M. Xu, P. Tieu, C. Lee, J. Cai, H. M. Lee, X. Pan, X. Duan, W. A. Goddard and Y. Huang, *Nat. Catal.*, 2020, **3**, 804–812.
19 M.-Y. Lee, S. Ringe, H. Kim, S. Kang and Y. Kwon, *ACS Energy Lett.*, 2020, **5**, 2987–2994.
20 M. G. Kibria, C.-T. Dinh, A. Seifitokaldani, P. De Luna, T. Burdyny, R. Quintero-Bermudez, M. B. Ross, O. S. Bushuyev, F. P. García de Arquer, P. Yang, D. Sinton and E. H. Sargent, *Adv. Mater.*, 2018, **30**, 1804867.
21 S. Sultan, J. Hyun Kim, S. Kim, Y. Kwon and J. Sung Lee, *J. Energy Chem.*, 2021, **60**, 410–416.
22 S. Mou, Y. Li, L. Yue, J. Liang, Y. Luo, Q. Liu, T. Li, S. Lu, A. M. Asiri, X. Xiong, D. Ma and X. Sun, *Nano Res.*, 2021, **14**, 2831–2836.
23 Y. Zhou, F. Che, M. Liu, C. Zou, Z. Liang, P. De Luna, H. Yuan, J. Li, Z. Wang, H. Xie, H. Li, P. Chen, E. Bladt, R. Quintero-Bermudez, T.-K. Sham, S. Bals, J. Hofkens, D. Sinton, G. Chen and E. H. Sargent, *Nat. Chem.*, 2018, **10**, 974–980.
24 A. Loiudice, P. Lobaccaro, E. A. Kamali, T. Thao, B. H. Huang, J. W. Ager and R. Buonsanti, *Angew. Chem., Int. Ed.*, 2016, **55**, 5789–5792.
25 D. Gao, I. Sinev, F. Scholten, R. M. Arán-Ais, N. J. Divins, K. Kvashnina, J. Timoshenko and B. Roldan Cuenya, *Angew. Chem., Int. Ed.*, 2019, **58**, 17047–17053.
26 J. Kim, W. Choi, J. W. Park, C. Kim, M. Kim and H. Song, *J. Am. Chem. Soc.*, 2019, **141**, 6986–6994.
27 L. Fan, C. Xia, F. Yang, J. Wang, H. Wang and Y. Lu, *Sci. Adv.*, 2020, **6**, eaay3111.
28 A. Herzog, A. Bergmann, H. S. Jeon, J. Timoshenko, S. Kühl, C. Rettenmaier, M. Lopez Luna, F. T. Haase and B. Roldan Cuenya, *Angew. Chem., Int. Ed.*, 2021, **60**, 7426–7435.
29 Y. Lum and J. W. Ager, *Energy Environ. Sci.*, 2018, **11**, 2935–2944.
30 O. A. Baturina, Q. Lu, M. A. Padilla, L. Xin, W. Li, A. Serov, K. Artyushkova, P. Atanassov, F. Xu, A. Epshteyn, T. Brintlinger, M. Schuette and G. E. Collins, *ACS Catal.*, 2014, **4**, 3682–3695.
31 B. Zhang, J. Zhang, M. Hua, Q. Wan, Z. Su, X. Tan, L. Liu, F. Zhang, G. Chen, D. Tan, X. Cheng, B. Han, L. Zheng and G. Mo, *J. Am. Chem. Soc.*, 2020, **142**, 13606–13613.
32 S. Y. Lee, H. Jung, N.-K. Kim, H.-S. Oh, B. K. Min and Y. J. Hwang, *J. Am. Chem. Soc.*, 2018, **140**, 8681–8689.
33 H. Mistry, A. S. Varela, C. S. Bonifacio, I. Zegkinoglou, I. Sinev, Y.-W. Choi, K. Kisslinger, E. A. Stach, J. C. Yang, P. Strasser and B. R. Cuenya, *Nat. Commun.*, 2016, **7**, 12123.
34 D. Ren, Y. Deng, A. D. Handoko, C. S. Chen, S. Malkhandi and B. S. Yeo, *ACS Catal.*, 2015, **5**, 2814–2821.
35 L. Li, L. Shi, X. Yu, S. Qing, Z. Gao, Q. Luo, G. Feng and R. Zhang, *Chin. Chem. Lett.*, 2019, **30**, 1147–1152.
36 D. Kim, C. Xie, N. Becknell, Y. Yu, M. Karamad, K. Chan, E. J. Crumlin, J. K. Nørskov and P. Yang, *J. Am. Chem. Soc.*, 2017, **139**, 8329–8336.
37 F. Liu, C. Wu and S. Yang, *J. Phys. Chem. C*, 2017, **121**, 22139–22146.
38 F. Wang, K. Kusada, D. Wu, T. Yamamoto, T. Toriyama, S. Matsumura, Y. Nanba, M. Koyama and H. Kitagawa, *Angew. Chem., Int. Ed.*, 2018, **57**, 4505–4509.
39 M. T. Greiner, T. E. Jones, S. Beeg, L. Zwiener, M. Scherzer, F. Girgsdies, S. Piccinin, M. Armbrüster, A. Knop-Gericke and R. Schlögl, *Nat. Chem.*, 2018, **10**, 1008–1015.
40 R. Daiyan, T. Tran-Phu, P. Kumar, K. Iputera, Z. Tong, J. Leverett, M. H. A. Khan, A. Asghar Esmailpour, A. Jalili, M. Lim, A. Tricoli, R.-S. Liu, X. Lu, E. Lovell and R. Amal, *Energy Environ. Sci.*, 2021, **14**, 3588–3598.
41 S. Sultan, M. Ha, D. Y. Kim, J. N. Tiwari, C. W. Myung, A. Meena, T. J. Shin, K. H. Chae and K. S. Kim, *Nat. Commun.*, 2019, **10**, 5195.
42 Y. Kim, S. Park, S.-J. Shin, W. Choi, B. K. Min, H. Kim, W. Kim and Y. J. Hwang, *Energy Environ. Sci.*, 2020, **13**, 4301–4311.
43 M. Osawa, in *Near-Field Optics and Surface Plasmon Polaritons*, ed. S. Kawata, Springer Berlin Heidelberg, Berlin, Heidelberg, 2001, pp. 163–187, DOI: 10.1007/3-540-44552-8_9.
44 D. K. Lambert, *Electrochim. Acta*, 1996, **41**, 623–630.
45 C. M. Gunathunge, V. J. Ovalle, Y. Li, M. J. Janik and M. M. Waegele, *ACS Catal.*, 2018, **8**, 7507–7516.
46 C. M. Gunathunge, V. J. Ovalle and M. M. Waegele, *Phys. Chem. Chem. Phys.*, 2017, **19**, 30166–30172.
47 A. Eilert, F. Cavalca, F. S. Roberts, J. Osterwalder, C. Liu, M. Favaro, E. J. Crumlin, H. Ogasawara, D. Friebel, L. G. M. Pettersson and A. Nilsson, *J. Phys. Chem.*, 2017, **8**, 285–290.
48 A. Soon, T. Söhnel and H. Idriss, *Surf. Sci.*, 2005, **579**, 131–140.
49 A. Föhlisch, M. Nyberg, P. Bennich, L. Triguero, J. Hasselström, O. Karis, L. G. M. Pettersson and A. Nilsson, *J. Phys. Chem.*, 2000, **112**, 1946–1958.
50 J. Hu, D. Li, J. G. Lu and R. Wu, *J. Phys. Chem. C*, 2010, **114**, 17120–17126.
51 A. K. Mishra, A. Roldan and N. H. de Leeuw, *J. Phys. Chem. C*, 2016, **120**, 2198–2214.
52 T. K. Todorova, M. W. Schreiber and M. Fontecave, *ACS Catal.*, 2020, **10**, 1754–1768.
53 H. Kim, D. Shin, W. Yang, D. H. Won, H.-S. Oh, M. W. Chung, D. Jeong, S. H. Kim, K. H. Chae, J. Y. Ryu, J. Lee, S. J. Cho, J. Seo, H. Kim and C. H. Choi, *J. Am. Chem. Soc.*, 2021, **143**, 925–933.
54 C. W. Lee, S.-J. Shin, H. Jung, D. L. T. Nguyen, S. Y. Lee, W. H. Lee, D. H. Won, M. G. Kim, H.-S. Oh, T. Jang, H. Kim, B. K. Min and Y. J. Hwang, *ACS Energy Lett.*, 2019, **4**, 2241–2248.
55 Y.-J. Zhang, V. Sethuraman, R. Michalsky and A. A. Peterson, *ACS Catal.*, 2014, **4**, 3742–3748.

 This journal is © The Royal Society of Chemistry 2022

Published on 22 March 2022. Downloaded by Ulsan National Institute of Science & Technology (UNIST) on 4/25/2022 10:19:47 AM.

56 M. Ma, E. L. Clark, K. T. Therkildsen, S. Dalsgaard, I. Chorkendorff and B. Seger, *Energy Environ. Sci.*, 2020, **13**, 977–985.
57 G. Kresse and J. Furthmüller, *Comput. Mater. Sci.*, 1996, **6**, 15–50.
58 G. Kresse and J. Furthmüller, *Phys. Rev. B: Condens. Matter Mater. Phys.*, 1996, **54**, 11169–11186.
59 J. P. Perdew, K. Burke and M. Ernzerhof, *Phys. Rev. Lett.*, 1996, **77**, 3865–3868.
60 M. Methfessel and A. T. Paxton, *Phys. Rev. B: Condens. Matter Mater. Phys.*, 1989, **40**, 3616–3621.
61 K. Mathew, R. Sundararaman, K. Letchworth-Weaver, T. A. Arias and R. G. Hennig, *J. Phys. Chem.*, 2014, **140**, 084106.
62 K. Momma and F. Izumi, *J. Appl. Crystallogr.*, 2011, **44**, 1272–1276.